Structural Basis of Substrate Selectivity and Catalysis in the Mycobacterial Long-Chain Acyl-CoA Carboxylase

Ajit Yadav[1], Nicole Rizzetto[1], Bogdan I. Florea[1], Sebastian Geibel[1,*]

Leiden Institute of Chemistry, Leiden University, Leiden, Netherlands.

[1] Leiden Institute of Chemistry, University of Leiden

*corresponding author: s.r.j.geibel@lic-leidenuniv.nl

Abstract

Long-chain acyl-CoA carboxylase (LCC) is an essential enzyme complex in mycobacteria that supplies acyl-CoA precursors for the biosynthesis of mycolic acids and complex lipids, yet its architecture, substrate selectivity, and conformational dynamics have remained poorly defined. Here we determine pre- and post-reaction states of the endogenous 868-kDa LCC complex from *Mycobacterium smegmatis* by cryo-electron microscopy at 2.1-3.7 Å resolution. These structures visualize ATP-dependent redistribution of the biotin carboxyl carrier protein and capture multiple substrate-free and substrate-engaged carboxyltransferase intermediates. LCC assembles into an asymmetric 8:2:4:2 organization of AccA3, AccD4, AccD5, and AccE5, with two biotin carboxylase modules flexibly tethered to a heterohexameric carboxyltransferase core. We define the structural basis of substrate selectivity within the CT core: AccD5 selectively binds the short-chain substrate C3-CoA, whereas AccD4 accommodates the long-chain substrate C16-CoA only in an open conformation. Unexpectedly, AccD4 in its closed conformation also engages and positions C3-CoA, revealing previously unrecognized conformational plasticity in substrate recognition. Together, these structural intermediates establish a mechanistic framework for LCC function, explaining how chemically distinct acyl-CoA substrates are processed within a single complex and revealing features that may contribute to the regulation of carbon flux into mycobacterial lipid biosynthesis.

Introduction

A hallmark of mycobacteria, including major pathogens such as *Mycobacterium tuberculosis* and *Mycobacterium abscessus* as well as environmental species such as *Mycobacterium smegmatis*, is a highly impermeable, lipid rich outer membrane known as the mycomembrane[1,2,3]. This barrier underlies intrinsic antibiotic tolerance, environmental resilience, and, in *M. tuberculosis*, long term persistence within the host[4,5]. Maintenance of mycomembrane integrity depends on the biosynthesis of mycolic acids, long α-alkyl, β-hydroxy fatty acids whose extreme chain length and structural complexity require specialized metabolic machinery[6,7,8]. In addition to mycolic acids, the mycomembrane contains diverse complex lipids that contribute to envelope architecture and permeability, and whose biosynthesis depends on the availability of acyl-CoA precursors[7].

In *M. tuberculosis*, the long chain acyl CoA carboxylase complex (LCC) catalyzes Cα-carboxylation reactions that generate two essential precursor pools for mycolic acid and complex lipid biosynthesis. These include the production of methylmalonyl CoA extender units required for multimethyl branched cell envelope lipids such as phthiocerol dimycocerosates, and the carboxylation of long chain acyl CoAs that supply the α branch precursors of mycolic acids[9,10,11]. Through these reactions, LCC constitutes a critical metabolic bottleneck linking central carbon metabolism to cell envelope lipid production. Catalysis proceeds via the canonical two step, biotin dependent mechanism, in which ATP driven carboxylation of biotin on the biotin carboxyl carrier protein by the biotin carboxylase activity is followed by carboxyl transfer to an acyl CoA substrate at the carboxyltransferase active site[12,13].

LCC assembles the biotin-dependent carboxylase AccA3, two carboxyltransferases AccD4 and AccD5, and the essential ε subunit AccE5 into a multifunctional enzyme complex[10]. Within this complex, long chain acyl CoAs ranging from C16 to C26 are processed by AccD4[14,15], whereas short chain substrates, including acetyl-CoA and propionyl-CoA, are processed by AccD5[11,15,16]. Despite its central role in mycobacterial physiology, key properties of the endogenous LCC, including subunit stoichiometry, overall architecture, conformational dynamics, biotin carboxyl carrier protein (BCCP) trafficking, and the molecular basis of dual chain length specificity, have remained unresolved. Structural insight has so far been limited to isolated components, including an AccA3 dimer and an AccD5 hexamer [11,17]. To address these gaps, we determined high-resolution structures of endogenous LCC from *M. smegmatis*, a close relative

of *M. tuberculosis*, across multiple catalytic states using single-particle cryo-electron microscopy.

Results

Serendipitous overproduction of endogenous LCC in *M. smegmatis* enables purification of the native complex

LCC was unexpectedly detected during StrepTactin pulldown experiments from *M. smegmatis* carrying an empty pMyNT plasmid (Fig. 1a). Owing to the covalently biotinylated AccA3 subunit, native LCC was purified directly from *M. smegmatis* lysate by StrepTactin affinity chromatography followed by size-exclusion chromatography. Notably, acetamide induction markedly increased LCC yield, whereas only low amounts were obtained from uninduced cells.

Endogenous LCC is catalytically active

Purified endogenous LCC exhibited catalytic activity in both half-reactions of its catalytic cycle. ATPase activity was highest in the presence of propionyl-CoA (C3) and progressively lower with the long-chain substrates palmitoyl-CoA (C16) and lignoceroyl-CoA (C24) (Fig. 1b). Quantitative liquid chromatography-mass spectrometry (LC-MS) analysis revealed a broad but discontinuous substrate specificity, with robust carboxylation of short-chain (C2, C3) acyl-CoAs and long-chain (C10-C16) acyl-CoAs (Fig. 1c; Supplementary Fig. 1). By contrast, activity toward the medium-chain substrate hexanoyl-CoA (C6) was detectable but below the limit of quantification, while octanoyl-CoA (C8) showed only minimal activity. Carboxylation of substrates longer than C16 was detectable but could not be quantified due to strong retention on the LC column (Supplementary Fig. 1-2). The observed substrate specificity profile closely mirrors that reported for reconstituted *M. tuberculosis* LCC [10].

In *M. smegmatis*, AccD5 supplies both malonyl-CoA[15] and methylmalonyl-CoA[11] via carboxylation of C2-CoA and C3-CoA, respectively, but the intrinsic substrate preference of LCC has not been defined. To investigate substrate preference, we performed LC-MS-based competition assays that showed carboxylation of C2-CoA was significantly reduced in the presence of C3-CoA, whereas carboxylation of C3-CoA was largely unaffected by C2-CoA, indicating a preference for propionyl-CoA over acetyl-CoA under these conditions (Fig. 1d).

LCC adopts a modular and highly dynamic structural architecture

To capture mechanistic states along the LCC catalytic cycle, we determined cryo-EM structures of cytosolic LCC in the presence of C16-CoA alone, a mixture of C3- and C16-CoA, or C16-CoA with ATP to induce turnover. A composite cryo-EM reconstruction of C16-CoA-bound LCC at avarage resolution of 3.1 Å revealed a modular architecture comprising a central carboxyltransferase (CT) core tethered to two mobile biotin carboxylase (BC) modules via the flexible, non-catalytic linker subunit AccE5, representing a pre-activation state in the absence of ATP (Fig. 2a, Supplementary Fig. 3-4, Supplementary table 1, 3). This reconstruction defines an overall stoichiometry of eight AccA3 subunits, two AccD4 subunits, four AccD5 subunits, and two AccE5 subunits (8:2:4:2).

The CT module harbours six active sites

The CT module, which catalyses transfer of CO_2 from carboxybiotin to acyl-CoA substrates, forms a pseudo-D3-symmetric double-ring assembly composed of one AccD4 dimer and two AccD5 dimers arranged as a trimer of dimers (Fig. 2b). AccD4 and AccD5 both adopt the canonical crotonase fold and are highly similar in structure (Z-score 22.8; RMSD 1.11 Å over 494 residues; Supplementary Fig. 5), giving rise to the apparent pseudo-symmetry. This architecture generates six carboxyltransferase active sites, with two located at the AccD4-AccD4 homodimer interfaces and four at the AccD5-AccD5 homodimer interfaces, where N- and C-terminal domains from adjacent protomers form the catalytic centers.

AccE5 tethers the BC and CT modules through a bipartite anchoring mechanism

AccE5 links the CT core to the BC modules through two interfaces. Its C-terminal helix-turn-helix motif inserts into the CT-ring lumen and contacts AccD4 and AccD5 protomers (Fig. 2b). At the N terminus, AccE5 anchors to each BC tetramer through a helix-in-a-β-cage interface, in which two β-strands from each AccA3 protomer and one from AccE5 form a nine-stranded β-barrel enclosing the AccE5 helix (Fig. 2c). A long intrinsically disordered region, unresolved in the density, separates the two interfaces and permits flexible BC-CT pivoting required for BCCP shuttling.

BCCP occupies distinct BC-anchored and CT-proximal states before activation

Within each BC module, AccA3 assembles as a tetramer (Fig. 2c) with a conserved ATP-grasp fold, comprising a catalytic BC core, a flexible ATP cap domain (residues 143-211 unresolved), and a BCCP domain that carries the biotin prosthetic group and is tethered by a flexible, mostly unresolved linker that enables shuttling of carboxybiotin from the BC module to the CT core.

One BCCP is resolved per BC tetramer, with the biotinylated Lys564 inserted into the ATP-binding pocket in a pre-activation pose poised for ATP-dependent carboxylation (Fig. 2d). A short linker segment contacts the AccD4 dimer, positioning this BC-anchored BCCP proximal to the CT module, primarily via residues K512 and R517, which form salt bridges and hydrogen bonds with AccD4 (Fig. 2b).

In addition to these BC-anchored BCCPs, four further BCCPs are observed near the AccD5-facing surface of the CT core (Fig. 2a). These CT-proximal BCCPs show partial density, whereas the uncarboxylated biotin moiety is well defined as it samples the active-site entrance, consistent with transient, non-productive docking (Fig. 2e). Linker density is unresolved for these CT-bound BCCPs, precluding assignment to specific AccA3 subunits, and two additional BCCPs remain undetected, consistent with high mobility. Notably, despite the presence of C16-CoA in AccD4, no BCCP engages the AccD4 active site under ATP-free conditions, indicating preferential sampling between the BC module and AccD5.

AccD4 adopts open and closed conformations that gate long-chain substrate access

Three-dimensional variability analysis revealed conformational flexibility within the CT core (Supplementary Video 1). We therefore resolved the principal components by non-uniform refinement (Supplementary Fig. 3, 6; Supplementary Table 2-3). This strategy yielded two CT-core reconstructions at 2.3 Å and 2.9 Å resolution, revealing that AccD4 samples two principal conformations characterized by coordinated gating of the acyl-chain tunnel and the CoA-binding region (Fig. 3a). In the open conformation, the acyl-chain tunnel is widened and accommodates a well-defined C1-C16 segment of the substrate C16-CoA (Fig. 3b), whereas the CoA moiety is poorly resolved, with weak density observed for the S1P-C7P segment and fragmented density for the adenine ring, indicating flexibility of the CoA moiety (Fig3b; Supplementary Fig. 7). Accordingly, in the open conformation AccD4 engages C16-CoA primarily through a tight network of van der Waals interactions surrounding the acyl chain (Fig. 3b).

By contrast, in the closed, C16-CoA-free conformation, the region proximal to the CoA moiety contracts (Fig. 3c). The α-helix spanning residues 433-443 of AccD4 converts into a loop that shifts inward, repositioning L439 together with a preceding loop harboring I431 into the space occupied by the C6-N4P region in the open state. On the opposing AccD4' protomer, an inward shift of the loop spanning residues 126'-136' places I133' into the region that accommodates the C1-S1P segment in the open conformation. Although these movements narrow the substrate path, they do not fully occlude it. However, an inward movement of helix 404-409 constricts the acyl-chain tunnel, reducing the G170'-G405 H-H distance to ~4.5-4.7 Å—below the ~5.2 Å steric minimum required to accommodate a ~3 Å acyl chain (Fig. 3d). Accordingly, C16-CoA is not observed in the AccD4 closed conformation as it would create steric clashes.

ATP turnover drives BCCP redistribution between substrate-engaged and product-release states

To examine LCC during ATP turnover, we analyzed C16-CoA-bound LCC in the presence of ATP and obtained two composite reconstructions corresponding to distinct catalytic intermediates.

The first reconstruction, refined to an average resolution of 2.9 Å, reveals that ATP induces redistribution of the biotin carboxyl carrier protein BCCP (Fig. 4a; Supplementary Fig. 8-9; Supplementary Tables 4, 6). BCCPs dissociate from the BC tetramers, where density consistent with bound ADP is observed in the AccA3 active sites, indicating a post-carboxylation state of the BC module (Fig. 4b, c). This density was assigned as ADP coordinated by Mg^{2+} based on structural superposition with the structurally similar biotin carboxylase from *Escherichia coli* resolved in complex with ADP-Mg^{2+} (PDB ID 3RV3; 0.92Å, over 344 residues; Supplementary Fig. 10).

Under turnover conditions, the carrier domains instead associate with AccD4, which adopts an open, substrate-engaged conformation (Fig. 4a). No BCCP density is detected at AccD5, indicating preferential association of BCCP with substrate-bound AccD4 (Fig. 4a; Supplementary Video 2). Compared with the ATP-free pre-activation state, BCCP density at C16-CoA-bound AccD4 is markedly more diffuse, consistent with rapid shuttling between the BC and CT modules. The biotinylated linker lysine is not resolved, suggesting fast insertion and withdrawal cycles during catalysis. Consistent with this dynamic behavior, no density corresponding to a carboxylated C2 position of C16-CoA is observed (Supplementary Fig. 11).

The second reconstruction, refined to an average resolution of 3.2 Å, captures a post-reaction state in which density for ADP is retained, whereas BCCP and C16-CoA are absent, consistent with a product-release intermediate (Fig. 4d; Supplementary Fig. 12-13; Supplementary Table 5-6).

Structural comparison of the substrate-engaged and product-release intermediates reveals that the BC tetramers rotate relative to the CT core, a motion that may facilitate delivery of the newly carboxylated BCCP to the AccD4 active site while simultaneously repositioning decarboxylated BCCP for re-engagement with the BC module (Supplementary Fig. 14).

Long- and short-chain substrates are simultaneously accommodated by AccD4 and AccD5

Next, we analyzed the pre-activation state of LCC in the presence of both C3- and C16-CoA in the absence of ATP (Supplementary Fig. 15). The resulting reconstructions reveal simultaneous binding of C16-CoA at AccD4 and C3-CoA at AccD5, yielding an overall architecture that closely resembles the ATP-free, C16-CoA-bound pre-activation state.

For the majority of particles, only the CT core could be resolved to high resolution (2.2 Å), whereas the flexible BC tetramers remained poorly defined. However, a minor particle population yielded a composite reconstruction (Supplementary Fig. 16; Supplementary Table 7, 9). In this structure, four BCCP domains localize near the four C3-CoA-engaged AccD5 active sites (Fig. 5a), while no BCCP density is detected at the two C16-CoA-bound AccD4 sites, consistent with the C16-CoA-bound pre-activation state of LCC.

Both BC tetramers tilt toward the CT core and adopt a more pronounced inclination than observed in the C16-CoA-only pre-activation state. Within each BC tetramer, one BCCP and its associated linker contact an AccD4 protomer. The biotinylated Lys564, however, remains oriented toward the BC active site and poised for carboxylation (Supplementary Fig. 17), consistent with the pre-activation configuration observed for C16-CoA-bound LCC (Fig. 2d).

Structural basis of C3-CoA recognition by AccD5

We next examined how the CT module engages the short-chain substrate C3-CoA at AccD5. Density for C3-CoA is well resolved, with the CoA moiety adopting a compact, bent conformation (Fig. 5b). The adenine base is coordinated by hydrogen bonds to backbone carbonyls of S116, A146, A148 and I150 is further positioned by an aromatic interaction with F462. The C1 carbonyl of the acyl chain is stabilized by hydrogen bonds from A148 and G187.

AccD4 substrate selectivity is governed by conformational state

Three-dimensional variability analysis[18] of the CT core followed by non-uniform refinement (Supplementary Fig. 15, 18; Supplementary Tables 8-9) revealed two AccD4 active-site conformations with distinct substrate preferences (Supplementary Video 3). In the open conformation, AccD4 binds C16-CoA, while C3-CoA is observed exclusively at AccD5 with well-defined density (Supplementary Fig. 19a; Fig. 5b); under these conditions, BCCP density is detected at AccD5 but not at AccD4. By contrast, when AccD4 adopts the closed conformation, which sterically excludes long-chain substrates, it accommodates C3-CoA (Fig. 5c). In this state, diffuse BCCP density appears at AccD4 and is lost at AccD5 (Supplementary Video 3-4), while C3-CoA density at AccD5 becomes less defined (Supplementary Fig. 19b), indicating reduced occupancy and suggesting competition between the two CT protomers for the short-chain substrate.

Within the closed AccD4 active site, the short acyl chain is stabilized by van der Waals interactions, the CoA phosphate forms a salt bridge with K166, and L439 contributes to positioning the adenine base in a manner analogous to Phe462 in AccD5. The conserved glycine pair G169-G170 occupies the oxyanion-hole position adjacent to the C2 carboxylation site, completing a catalytically competent architecture for short-chain substrates. Together, these observations indicate that AccD4 substrate selectivity is regulated by conformational state. Short-chain substrates can be productively engaged in the closed conformation, whereas long-chain substrates such as C16-CoA are accommodated only in the open conformation.

Structural determinants of substrate selectivity in AccD4 and AccD5

To understand how the two CT subunits discriminate between acyl-CoA substrates, we compared the active-site architectures of AccD4 in its C16-bound state with AccD5 in its C3-bound state. Although both enzymes possess hydrophobic pockets of similar overall topology, only AccD4 undergoes conformational widening of the acyl-chain binding pocket required to accommodate a long C16 acyl chain without steric clashes. In contrast, the CoA-binding site of AccD5 displays limited conformational flexibility (Supplementary Videos 1-3), such that extension of a long acyl chain would result in steric conflict with surrounding residues, precluding binding (Fig. 6a). In particular, a constriction at the interface of two opposing

AccD5 protomers, defined by residues G187′ and G428, prevents deeper penetration of longer acyl chains (Fig. 6b).

AccD4 in its open conformation engages C16-CoA predominantly through extensive van der Waals interactions along the acyl chain, with few contacts to the CoA moiety (Fig. 3b, Supplementary Fig. 7). By contrast, AccD5, whose binding pockets lacks sufficient volume for long-chain substrates, bind C3-CoA through interactions with the short acyl chain, but primarily through the CoA group (Fig. 5b). These differences in pocket accessibility and substrate interaction explain why AccD4 in its open conformation, but not AccD5 can accommodate long-chain acyl-CoA substrates (Fig. 6c).

Conserved catalytic architecture with differential substrate positioning

Structural comparison of the AccD4 and AccD5 with the PccB from *Streptomyces coelicolor* bound to C3-CoA and biotin (PDB ID 1XNY) identifies two conserved glycine-based oxyanion holes in AccD4 and AccD5, required for carboxyl transfer (Fig. 7a-b). Oxyanion hole 1 (G169′-A170′ in AccD4; G186'-G187' in AccD5) is positioned to stabilize the substrate enolate following α-proton abstraction, whereas oxyanion hole 2 (G405-G406 in AccD4; G428-A429 in AccD5) is positioned to stabilize the carboxylate of carboxybiotin during CO_2 transfer. In both, C3-CoA engaged AccD4 and AccD5, the C2 position of bound C3-CoA aligns with these conserved oxyanion holes (Fig. 7c-d). Despite this conserved architecture, the α-carbon of C16-CoA in AccD4 remains > 10 Å from the catalytic center (Fig. 7e), compared with the ~3 Å separation observed in transfer-competent PccB structures. Thus, long-chain carboxylation by AccD4 requires an additional conformational rearrangement to bring the acyl substrate into a transfer-competent geometry, which is not resolved in the present structures. In summary, the structures presented here capture a series of conformational and catalytic intermediates of LCC across pre-activation, turnover, and post-reaction conditions. The experimentally resolved intermediates and their relationships are summarized schematically in Figure 8.

Discussion

In this work, we define the architecture and conformational dynamics of the mycobacterial long-chain acyl-CoA carboxylase and reveal the structural basis for dual substrate selectivity mediated by conformational gating. The LCC architecture differs markedly from that of known bacterial and eukaryotic acyl-CoA carboxylase complexes[19,20-22]. Whereas canonical acetyl-

CoA carboxylases adopt a symmetric 6:6 organization[19-21,23] in which six BC domains pair with six CT active sites, LCC is asymmetric, comprising eight BC active sites arranged as two AccA3 tetramers but only six CT sites formed by a 2:4 AccD4/AccD5 heterohexamer. This 8:6 mismatch is unprecedented among biotin-dependent carboxylases.

A second distinguishing feature of LCC is the presence of two AccE5 subunits that flexibly tether each BC module to the CT ring. No comparable anchoring mechanism exists in other ACCs, in which BC and CT assemblies associate through direct, symmetric interfaces. These architectural deviations correlate with the expanded substrate range of LCC, which accommodates both short-chain and very long-chain acyl-CoA substrates via the specialized AccD5 and AccD4 active sites, respectively. In contrast, symmetric ACCs typically carboxylate a single substrate class, establishing LCC as a structurally and mechanistically distinct member of the ACC family.

Despite its unconventional architecture, LCC undergoes conformational transitions that follow principles established for bacterial biotin-dependent carboxylases. ATP binding promotes redistribution of BCCP from the ADP bound BC module toward the CT region, consistent with long range biotin shuttling described for pyruvate carboxylase[24]. As observed in human acyl CoA carboxylases, ligand binding remodels the CT pocket, with apo states remaining open and substrates inducing closure[23].

AccD4 extends this canonical behavior by enabling conformation-dependent substrate specificity. It alternates between open and closed states that permit or restrict long-chain substrate engagement, thereby providing a mechanism to regulate long-chain acyl-CoA carboxylation without changes in complex composition. In contrast to other biotin-dependent carboxylases, where gating primarily controls access to a single substrate class, AccD4 exploits this principle to impose substrate-selective catalysis.

We further show that short-chain substrates, C2-CoA and C3-CoA, compete for shared catalytic sites within the LCC complex, with propionyl-CoA preferentially retained over acetyl-CoA. Together, these findings indicate that substrate utilization by LCC is governed by both the relative intracellular availability of short-chain substrates and, for long-chain substrates, by conformational gating of the carboxyltransferase sites.

Having established the conformational behavior of the CT module, we find that its catalytic architecture is conserved. As in other biotin-dependent carboxylases, both AccD4 and AccD5 contain two glycine-based oxyanion holes. In the C3-CoA-bound AccD4 and AccD5 structures,

the distances between the (yet uncarboxylated) C2 carbon of C3-CoA and oxyanion hole 1 fall within the range compatible with CO_2 transfer from carboxybiotin (2.8 Å / 4.8 Å for AccD4 and 3.4 Å / 4.4 Å for AccD5), comparable to values reported for PccB (3.4 Å / 4.0 Å). In contrast, for C16-CoA this distance remains substantially larger (>10 Å) in all captured states, indicating that these conformations are not competent for carboxyl transfer. Given the highly dynamic nature of the carboxyltransfer reaction, we propose that a short-lived rearrangement, not resolved in our structures, is required to align carboxybiotin with the α-carbon of C16-CoA and thereby enable catalysis.

Whereas we were unable to observe the short-lived carboxylated biotin at the CT active site under ATP-turnover conditions, we do observe sampling of the CT active site by the uncarboxylated biotin moiety of BCCP in the absence of ATP (Fig. 2a,e). In these pre-transfer states, the distance between the uncarboxylated biotin and oxyanion hole 2 is approximately 8-8.5 Å, substantially larger than the ~2.9-3.0 Å separation required for productive carboxyl transfer, as established for PccB from *Streptomyces coelicolor*[25] (Fig. 7b) . Consistent with this interpretation, structural studies across biotin-dependent carboxylases, including *S. aureus* enzymes[26] and human ACC[27], have shown that covalently linked biotin can adopt either distal (exo) or proximal (endo) conformations relative to the catalytic center, with only the proximal state being competent for carboxyl transfer.

Finally, we find that the core architecture of LCC is conserved across mycolic-acid producing Corynebacteriales, indicating that the mechanistic model described here is broadly applicable. Phylogenetic analysis of the core subunits AccA3, AccD4, AccD5, and AccE5 reveals conservation across major human pathogens, including *Mycobacterium tuberculosis*, *M. abscessus*, and *M. leprae*, as well as animal-associated species and the industrial actinobacterium *Corynebacterium glutamicum* (Supplementary Fig. 20-21). Consistent with this conservation, AlphaFold3[28] based modelling of LCC assemblies from representative species, using the stoichiometry defined by our cryo-EM structure, yields high confidence predictions for the BC and CT modules, supporting conservation of LCC architecture and mechanism in both pathogenic and industrial species.

Together, the findings establish LCC as a modular and dynamic carboxylase complex and provide a structural framework for understanding how substrate routing and carbon flux into mycolic-acid and complex-lipid biosynthesis may be regulated in mycobacteria.

Methods

Bacterial strains and growth conditions

Mycobacterium smegmatis mc²155 was transformed with the plasmid pMyNT empty vector under the control of the acetamidase promoter. Cultures were grown in Luria-Miller (LB) broth supplemented with 0.2% (v/v) glycerol at 180 rpm. Expression was induced with 0.2% (w/v) acetamide at an optical density at 600 nm (OD_{600}) of 0.5, and cells were harvested at a final OD_{600} of 2.0-2.1. Cells were collected by centrifugation and washed three times with phosphate-buffered saline (PBS). As a control, uninduced pMyNT empty-vector cultures were processed in parallel under identical conditions.

Purification of the LCC complex

Cell pellets from induced and uninduced pMyNT empty-vector cultures were resuspended at a 1:5 (w/v) ratio in buffer A (300 mM NaCl, 50 mM HEPES, 1 mM DTT, pH 8.0) supplemented with EDTA-free protease inhibitors (Roche) and lysozyme (Roche). Cells were lysed by three passages through an Emulsiflex-C3 homogenizer (Avestin), and unlysed material was removed by centrifugation at 10,000 × g for 15 min at 4 °C.

The soluble fraction was separated by ultracentrifugation at 45,000 rpm for 1 h at 4 °C using a 45Ti rotor and applied directly to a pre-equilibrated Strep-Tactin™ XT 4Flow™ column (IBA). The column was washed with buffer A until a stable UV baseline was achieved, and bound proteins were eluted with buffer B (buffer A supplemented with 50 mM biotin, pH 8.0). Eluted samples were further purified by size-exclusion chromatography on a Superose 6 Increase 10/300 GL column (GE Healthcare) equilibrated in buffer C (300 mM NaCl, 20 mM HEPES, 1 mM DTT, pH 8.0). Fractions were analyzed by SDS-PAGE and BN-PAGE followed by colloidal Coomassie Blue staining.

In-gel digestion and nano-LC-MS workflow

Proteins were separated by reducing SDS-PAGE, stained with Coomassie Blue, and excised bands were cut into ~1 mm^3 pieces. In-gel digestion was performed as described by Li *et al*[29]. Gel pieces were washed repeatedly with acetonitrile (ACN) and water to remove SDS, reduced with 2 mM DTT (30 min, 37 °C), alkylated with 5 mM iodoacetamide (30 min, room

temperature, dark), and digested overnight at 37 °C with sequencing-grade trypsin (10 ng/µl; Promega) in 50 mM ammonium bicarbonate containing 1 mM $CaCl_2$. Peptides were extracted with ACN and ACN/ammonium bicarbonate, dried by vacuum centrifugation, resuspended in 97:3:0.1 (H_2O:ACN:formic acid), and desalted using C18 StageTips following standard protocols.

Desalted peptides were analyzed by nanoLC-MS/MS on an UltiMate 3000 RSLCnano system coupled to a Q Exactive HF mass spectrometer (Thermo Fisher Scientific). Peptides were separated using a trap-elute configuration with a nanoEase M/Z Symmetry C18 trap column (180 µm × 20 mm) and a nanoEase M/Z HSS C18 T3 analytical column (75 µm × 250 mm), maintained at 40 °C. Peptides were eluted over an 85 min gradient from 1% to 40% mobile phase B (0.1% formic acid in acetonitrile) at 0.3 µl/min.

The mass spectrometer was operated in positive-ion, data-dependent acquisition mode. Full MS scans were acquired at 60,000 resolution (m/z 200), followed by up to 10 MS/MS scans at 15,000 resolution using higher-energy collisional dissociation (normalized collision energy 28). Dynamic exclusion was set to 20 s, and singly charged and unassigned ions were excluded. Instrument performance was monitored using routine quality control injections.

Raw data were processed using MaxQuant (v1.6.17.0) with label-free quantification and match-between-runs enabled. Searches were performed against the UniProt reviewed database supplemented with common contaminants.

Cryo-EM sample preparation and data collection

To generate palmitoyl-CoA-bound LCC, LCC was incubated with 500 µM palmitoyl-CoA for 2h before vitrification. And for the palmitoyl-CoA bound complex under ATP turnover condition, samples were incubated with 500 µM palmitoyl-CoA, 25mM $NaHCO_3$, 10mM ATP, and 10mM $MgCl_2$ for 2h before vitrification. Propionyl- and palmitoyl-CoA-bound LCC was generated by addition of 1 mM propionyl-CoA and 500 µM palmitoyl-CoA.

Cryo-EM grids were prepared by applying 3.5 µl of sample to glow-discharged gold grids (R1.2/1.3, 300 mesh, Ultrafoil). Grids were blotted for 3.5 s with a blot force of 10 using a Vitrobot Mark IV (Thermo Fisher Scientific) operating at 4 °C and 100% relative humidity, followed by rapid vitrification in liquid ethane. Data were acquired on a Titan Krios G1 transmission electron microscope (Thermo Fisher Scientific) operating at 300 kV, equipped with a Gatan K3 direct electron detector and a BioQuantum energy filter (Gatan) with a 20eV

slit width. For the palmitoyl-CoA, palmitoyl-CoA under ATP turnover condition, and the mixture of propionyl-CoA and palmitoyl-CoA, a total of 14,716, 15,130, and 14,974 movies, respectively, were collected in electron counting mode using aberration-free image shift as implemented in EPU (Thermo Fisher Scientific). Movies were recorded at a nominal magnification of 105,000×, corresponding to a calibrated pixel size of 0.836 Å. Each movie was acquired over 60 frames with a total dose of 60 $e^{-}/Å^{2}$ and a defocus range of −0.8 to −2.0 µm.

Cryo-EM data processing

All the cryo-EM data were processed using CryoSPARC v4.5.3 and v4.7.1 (Structura Biotechnology Inc.). Patch-based motion correction and contrast transfer function (CTF) estimation were performed on all acquired micrographs[30]. Micrographs were manually curated, and a subset was used for initial particle picking. Manually selected particles were subjected to 2D classification, and high-quality class averages were used as templates for automated particle picking.

For the LCC complex incubated with palmitoyl-CoA cryo-EM data (Supplementary Fig.3), particles were extracted with a box size of 512 pixels and Fourier cropped to 220 pixels. Multiple rounds of 2D classification were performed to remove junk particles. An initial ab initio reconstruction was generated from selected particles, followed by iterative heterogeneous refinement to resolve compositional heterogeneity. Particles corresponding to the best-resolved classes were re-extracted with a box size of 480 pixels, Fourier cropped to 416 pixels, and subjected to non-uniform refinement[31]. This yielded consensus map at resolution 2.15 Å measured by gold-standard Fourier shell correlation at 0.143 criterion. The resulting map exhibited reduced resolution at the distal ends of the complex (AccA3 at top and bottom), attributed to conformational flexibility. To further improve the reconstruction, the non-uniform refinement map was used for mask generation. Density subtractions were employed to isolate the AccA3 at top, AccD5:AccD4:AccE5 at centre, and AccA3 at bottom regions. Focused refinement of the centre region (AccD5:AccD4:AccE5) yielded a locally refined map at 2.16 Å resolution.

Given the substantial conformational variability, 3D variability analysis[18] was performed on the AccD5:AccD4:AccE5, and the resulting principal components were analyzed in ChimeraX v1.9. Based on the principal component analysis, particles were subjected to 3D variability display (cluster mode) job in cryoSPARC v4.5.3 (Structura Biotechnology Inc.), and the best-

resolved classes were subjected to non-uniform refinement. This particle sorting strategy resulted in two distinct states of AccD5:AccD4:AccE5, where AccD4 is found in either a closed or an open state. The final reconstruction result in resolution 2.3 Å for closed state and 2.9 Å for open state (supplementary Fig. 6a, b), respectively, which were subsequently used for atomic model building. To resolve flexible AccA3, direct local refinement from particle subtractions of the flexible AccA3 at top and bottom regions did not produce substantial improvements. To solve this problem, the subtracted particles corresponding to these regions were subjected to ab initio reconstruction to generate three initial models. These models were used in heterogeneous refinement to classify the particle population. The best-resolved classes were further subjected to non-uniform refinement, resulting in improved density maps for the top and bottom regions. Final resolutions, determined at the gold-standard Fourier shell correlation (FSC) 0.143 criterion, were 3 Å and 3 Å, respectively (Supplementary Fig.6c,d), and were subsequently used to guide atomic model building. Further, to get full LCC map, 3D classification was performed on full set of particles from non-uniform refinement job. Class with 65,445 particles was selected where full LCC complex (4AccD5:2AccD4:8AccA3:2AccE5) could be resolved. These particles subjected to non-uniform refinement and further local refinement to get high resolution of AccA3 at top, AccD5:AccD4:AccE5 at centre, and AccA3 at bottom. The resulting locally refined maps were combined to generate a composite reconstruction of the full LCC complex (Supplementary Fig.4).

For the LCC complex incubated with palmitoyl-CoA, ATP, MgCl2, and NaHCO3 cryo-EM data (Supplementary Fig.8,12) particles were extracted with a box size of 480 pixels, Fourier cropped to 220 pixels. Multiple rounds of 2D classification were performed to remove junk particles. An initial ab initio reconstruction was generated from selected particles, followed by iterative heterogeneous refinement to resolve compositional heterogeneity. Particles of overexpressed views were removed by using the 'rebalance orientation' job. Balanced particles were re-extracted with a box size of 480 pixels, Fourier cropped to 416 pixels and subjected to non-uniform refinement. This yielded consensus map at 2.1 Å resolution (by gold-standard Fourier shell correlation at 0.143 criterion). The resulting map again exhibited reduced resolution at the distal ends of the complex (AccA3 at top and bottom), attributed to conformational flexibility. To further improve the reconstruction, the non-uniform refinement map was used for mask generation. Density subtractions were employed to isolate the AccA3

at top, AccD5:AccD4:AccE5 at centre , and AccA3 at bottom regions. Focused refinement of the centre region (AccD5:AccD4:AccE5) yielded a locally refined map at 2.1 Å. Given the substantial conformational variability, 3D variability analysis was performed on the AccD5:AccD4:AccE5 and the resulting principal components were analyzed in ChimeraX v1.9. Based on the principal component analysis, particles were subjected to 3D variability display (cluster mode) job in cryoSPARC v4.5.3 (Structura Biotechnology Inc.), and the best-resolved classes were subjected to non-uniform refinement, result in two clear distinct states of AccD5:AccD4:AccE5, where AccD4 exhibits closed and open states. The final reconstruction result in resolution 2.1 Å for closed state and 2.4 Å for open state, respectively, which were subsequently used for atomic model building. To resolve flexible AccA3, direct local refinement from particles subtraction of the flexible AccA3 at top and bottom regions did not produce substantial improvements. Then subtracted particles corresponding to these regions were subjected to ab initio reconstruction to generate three initial models. These models were used in heterogeneous refinement to classify the particle population. The best-resolved classes were further subjected to non-uniform refinement, resulting in improved density maps for the AccA3 at top and bottom regions. Final resolutions, determined at the gold-standard FSC 0.143 criterion, were 2.92 Å and 3.01 Å for AccA3 at top and AccA3 at bottom, respectively, and were subsequently used to guide atomic model building. Further, to get full LCC map, 3D classification was performed on full set of particles from non-uniform refinement. Two classes with 105,083 and 161,800 particles were selected where the full LCC complex (4AccD5:2AccD4:8AccA3:2AccE5) could be resolved. Further particles from both the classes were subjected to non-uniform refinement, and a similar workflow as above is followed to get high resolution of flexible AccA3 at top and bottom for both the classes. The resulting maps from both the classes were combined to make respective composite maps (Supplementary Fig. 9, 13). These two composite maps result in two clearly distinct states, where AccD4 are in closed and open state and AccA3 at bottom are rotated approximately by 80 degrees with respect to each other.

For the LCC complex incubated with propionyl-CoA and palmitoyl-CoA cryo-EM data (Supplementary Fig. 15), a similar workflow is followed. Particles were extracted with a box size of 480 pixels, Fourier cropped to 220 pixels. Multiple rounds of 2D classification were performed to remove junk particles. An initial ab initio reconstruction was generated from selected particles, followed by iterative heterogeneous refinement to resolve compositional

heterogeneity. Particles corresponding to the best-resolved classes were re-extracted with a box size of 480 pixels, Fourier cropped to 416 pixels and subjected to non-uniform refinement. This yielded consensus map at 2.1 Å resolution (by gold-standard Fourier shell correlation at 0.143 criterion). Again, the resulting map exhibited reduced resolution at the distal ends of the complex (AccA3 at top and bottom), attributed to conformational flexibility. To further improve the reconstruction, the non-uniform refinement map was used for mask generation. Density subtractions were employed to isolate the AccA3 at top, AccD5:AccD4:AccE5 at centre , and AccA3 at bottom regions. Focused refinement of the centre region (AccD5:AccD4:AccE5) yielded a locally refined map at 2.09 Å. Given the substantial conformational variability, 3D variability analysis was performed on the AccD5:AccD4:AccE5, and the resulting principal component were analyzed in ChimeraX v1.9. Based on the principal component analysis, particles were subjected to 3D variability display (cluster mode) job in cryoSPARC v4.5.3 (Structura Biotechnology Inc.), and the best-resolved classes were subjected to non-uniform refinement, result in again two clear distinct state of AccD5:AccD4:AccE5, where AccD4 exhibits closed and open states. The final reconstructions result in 2.2 Å resolution for the closed state and 2.5 Å for the open state respectively (Supplementary Fig. 18a,b), that were subsequently used for atomic model building. To resolve flexible AccA3, again direct local refinement from particles subtraction of the flexible AccA3 at top and bottom regions did not produce substantial improvements. Then subtracted particles corresponding to these regions were subjected to ab initio reconstruction to generate three initial models. These models were used in heterogeneous refinement to classify the particle population. The best-resolved classes were further subjected to non-uniform refinement, resulting in improved density maps for the top and bottom regions. Final resolutions, determined at the gold-standard Fourier shell correlation (FSC) 0.143 criterion, were 2.9 Å, and 3.0 Å respectively (Supplementary Fig. 18c,d), and were subsequently used to guide atomic model building. To get full LCC map, 3D classification was performed on full set of particles from non-uniform refinement. Class with 13,970 particles was selected where full LCC complex (4AccD5:2AccD4:8AccA3:2AccE5) could be resolved. These particles subjected to non-uniform refinement and further local refinement to get high resolution of AccA3 at top, AccD5:AccD4:AccE5 at centre, and AccAA3 at bottom. The resulting locally refined maps were combined to generate a composite reconstruction of the full LCC complex (Supplementary Fig. 16).

Model Building

An initial atomic model of the carboxyl transferase module (4AccD5:2AccD4:2AccE5) with AccD4 in open conformation was generated using ModelAngelo[32] and rigid-body fitted into the cryo-EM density in ChimeraX[33], followed by real-space refinement[34] in Phenix[35]. All side chains were manually inspected and adjusted, and missing loops and termini were built in Coot[36] wherever well-defined density was present. Residues lacking interpretable side-chain density were modelled using only the underlying secondary-structure geometry in Coot, and residues with no observable density were either assigned zero occupancy or omitted from the final model. In the AccD4 closed conformation within the carboxyltransferase module (4AccD5:2AccD4:2AccE5), the loops encompassing residues 64-67, 256-263, and 445-454 lack interpretable density and were therefore omitted from the model or assigned zero occupancy. For the flexible biotin carboxylase top and bottom module (4AccA3:1AccE5), individual AlphaFold models were used as starting templates, and each polypeptide chain was independently fitted into the corresponding EM density in ChimeraX. Subsequent real-space refinement was performed in Phenix, followed by manual inspection and adjustment in Coot to refine side chains and to build missing loops and termini where the density allowed reliable interpretation. The B domain (residues 139-210) and BCCP domain (residues 530-598) of AccA3 were included in the models only in regions where the EM density was sufficiently well resolved; in the absence of clear density, these segments were not modelled. All ligand molecules were placed into the EM density using Coot with monomer library restraints and refined in Phenix. To accurately describe the covalent linkage between Lys564 of the BCCP domain and biotin, a covalent bond definition was first introduced in ChimeraX, and a custom restraint describing the Lys-biotin covalent geometry was generated with the elbow in Phenix. This restraint was applied during the final rounds of real-space refinement.

Liquid chromatography/mass spectrometry

Separation of different chain-length acyl-CoAs was achieved by ion pairing-reverse phase high-performance liquid chromatography (IP-RP-HPLC) with an Agilent 1260 Infinity II instrument (Agilent Corporation, Santa Clara, CA, USA) using a NUCLEODUR EC C18 column (dimensions: 50mm x 4.6mm x 3µm). The flow rate was 1ml/min in gradient mode with following elution program: the column was equilibrated with mobile phase A [90% H_2O and 10% (v/v) 100mM ammonium acetate]. 10 µl of each sample was injected, and same elution

condition continued for 1.5 min, followed by 9 min gradient to mobile phase B [90% CH_3CN and 10% (v/v) 100mM ammonium acetate]. Afterward, the column was washed for 2 min with mobile phase B [90% CH_3CN and 10% (v/v) 100mM ammonium acetate], followed by 10 sec gradients to reach mobile phase A [90% H_2O and 10% (v/v) 100mM ammonium acetate] and holding 2 more minutes at this conditions to equilibrate the column before injection of the next sample.

Mass spectrometry was performed using an Agilent 6475 LC/TQ system (Agilent Technologies, Santa Clara, CA, USA) equipped with an AJS electrospray ionization (ESI) source, operated in positive ion mode. ESI parameters were optimized for acyl-CoA's detection as follows: Nebulizer pressure 20.0 psi, gas flow 10.0 L/min, dry heater 100 °C, capillary voltage 4,000 V. The target mass scan was set from 100 m/z to 1,500 m/z. The fragmentor voltage and collision energy for the tandem mass spectrometry were individually optimized for each acyl-CoA to maximize signal intensity and fragmentation efficiency.

***In vitro* LCC activity assay**

LCC enzymatic activity was quantified by detecting carboxylated acyl-CoA products using ion-pair reverse-phase high-performance liquid chromatography (HPLC) coupled to triple quadrupole mass spectrometry (TQMS/MS). Reactions were carried out in a total volume of 35 µl containing 50 mM HEPES (pH 7.2), 2 mM ATP, 8 mM $MgCl_2$, 50 mM $NaHCO_3$, and 50 µM acyl-CoA substrate. The reactions were initiated by the addition of purified LCC complex (final concentration 0.25 µM) and incubated at 30 °C for 4 h. To quench enzymatic activity, reaction mixtures were transferred to -80 °C, followed by denaturation at 70 °C for 10 min. After centrifugation, the resulting supernatant was collected for further analysis. An internal standard was added prior to injection, and 10 µl of the diluted reaction mixture was loaded onto the chromatographic column. Acyl-CoA species were separated by ion-pairing reverse-phase HPLC. Detection was performed on an Agilent 6475 LC/TQ system (Agilent Technologies, Santa Clara, CA, USA) equipped with an AJS electrospray ionization (ESI) source, operated in positive ion mode. For substrate competition assays, equimolar (50 µM) mixtures of acyl-CoA species with varying carbon chain lengths were included, and reactions were conducted similarly as described above except that reactions were quenched after 10 min.

Data Analysis

Quantitative analyses were performed as follows. Calibration curves were first generated for individual acyl-CoA standards (C3, C8, C10, C12, C14, and C16-CoA) to confirm linearity between chromatographic peak area and analyte concentration. Extracted-ion chromatogram peaks corresponding to carboxylated coenzyme A, uncarboxylated coenzyme A, and the internal standard were integrated using MassHunter Qualitative Analysis software v10.0 (Agilent Technologies, Santa Clara, CA, USA), and the resulting peak areas were exported to spreadsheets and further processed in GraphPad Prism 10 (GraphPad Software, San Diego, CA). All samples were analyzed in triplicate, and data are reported as mean values ± standard deviation.

ATPase activity assay

The ATP hydrolysis activity of the LCC complex was measured spectrophotometrically[37] by coupling ADP production to NADH oxidation using pyruvate kinase and lactate dehydrogenase. Oxidation of NADH was monitored at 340 nm in a microplate reader (FLUOstar Omega, BMG LABTECH). Reactions were carried out in a total volume of 80 µl in 384-well non-binding microplates (Greiner). The assay buffer contained 50 mM HEPES (pH 7.6), 50 mM $NaHCO_3$, 5 mM $MgCl_2$, 3 mM ATP, 0.5 mM phosphoenolpyruvate, 0.2 mM NADH, 0.3 mg/ml BSA, 4.8-8 units of pyruvate kinase, 7.2-11.2 units of lactate dehydrogenase, and the desired concentration of acyl-CoA. Reactions were initiated by addition of purified LCC complex to a final concentration of 0.125 µM. Assays were performed at 30 °C using preincubated plates.

Structure predictions

The structures of the 4AccD5:2AccD4:2AccE5 and 4AccA5:1AccE5 complexes from different *Mycobacteria* and *Corynebacteria* species were predicted using AlphaFold3[28] (DeepMind, 2025 release). Protein sequences were retrieved from UniProt and submitted to AlphaFold3 with the appropriate stoichiometry and default settings. For each complex, among the five structural models generated, the model with the highest confidence was selected. The structures were visualized with UCSF ChimeraX 1.9[33]. Subunits were coloured according to the proposed scheme, and for the AccD4/AccD5/AccE5 complex the unstructured N-terminal region of AccE5 was removed for clarity.

Data and Material Availability

Cryo-EM maps and associated atomic models reported in this study have been deposited in the Electron Microscopy Data Bank under accession codes EMD-56274 (LCC complex bound to ADP, and Mg^{2+}, non-uniform refinement (consensus map)), EMD-56275 (LCC complex bound to ADP, and Mg^{2+}, non-uniform refinement (focused map of bottom BC module and centre CT module)), EMD-56276 (LCC complex bound to ADP, and Mg^{2+}, non-uniform refinement (focused map of top BC module and centre CT module)), EMD-56277 (LCC complex bound to ADP, and Mg^{2+}, local refinement (focused map of centre CT module), EMD-56278 (LCC complex bound to ADP, and Mg^{2+}, non-uniform refinement (focused map of bottom BC module)), EMD-56279 (LCC complex bound to ADP, and Mg^{2+}, non-uniform refinement (focused map of top BC module)), **EMD-56280** (LCC complex bound to ADP, and Mg^{2+}, composite map), EMD-56287 (LCC complex bound to palmitoyl-CoA, ADP, and Mg^{2+}, non-uniform refinement (consensus map)), EMD-56288 (LCC complex bound to palmitoyl-CoA, ADP, and Mg^{2+}, non-uniform refinement (focused map of top BC module and centre CT module)), EMD-56289 (LCC complex bound to palmitoyl-CoA, ADP, and Mg^{2+}, non-uniform refinement (focused map of bottom BC module and centre CT module)), EMD-56290 (LCC complex bound to palmitoyl-CoA, ADP, and Mg^{2+}, non-uniform refinement (focused map of top BC module)), EMD-56291 (LCC complex bound to palmitoyl-CoA, ADP, and Mg^{2+}, non-uniform refinement (focused map of bottom BC module)), EMD-56292 (LCC complex bound to palmitoyl-CoA, ADP, and Mg^{2+}, local refinement (focused map of centre CT module)), **EMD-56293** (LCC complex bound to palmitoyl-CoA, ADP, and Mg^{2+}, composite map), **EMD-56369** (BC top module (4AccA3:1AccE5) bound to ADP, and Mg^{2+}, non-uniform refinement of full data set), **EMD-56370** (BC bottom module (4AccA3:1AccE5) bound to ADP, and Mg^{2+}, local refinement of full data set), EMD-56301 (LCC complex bound to palmitoyl-CoA, non-uniform refinement (consensus map)), EMD-56302 (LCC complex bound to palmitoyl-CoA, non-uniform refinement (focused map of top BC module and centre CT module)), EMD-56303 (LCC complex bound to palmitoyl-CoA, non-uniform refinement (focused map of bottom BC module and centre CT module)), EMD-56304 (LCC complex bound to palmitoyl-CoA, local refinement (focused map of centre CT module)), EMD-56305 (LCC complex bound to palmitoyl-CoA, local refinement (focused map of top BC module sub volume 1)), EMD-56306 (LCC complex bound to palmitoyl-CoA, local refinement (focused map of top BC module sub volume 2)), EMD-56307 (LCC complex bound to palmitoyl-CoA, local refinement (focused map

of bottom BC module sub volume 1)), EMD-56308 (LCC complex bound to palmitoyl-CoA, local refinement (focused map of bottom BC module sub volume 2)), **EMD-56309** (LCC complex bound to palmitoyl-CoA, non-uniform refinement (composite map)), **EMD-56336** (Centre CT module (4AccD5:2AccD4:2AccE5) bound to palmitoyl-CoA, non-uniform refinement of cluster 1 from 3D variability analysis), **EMD-56359** (Centre CT module (4AccD5:2AccD4), non-uniform refinement of cluster 2 from 3D variability analysis), **EMD-56360** (BC top module (4AccA3:A1ccE5), non-uniform refinement of full data set), **EMD-56362** (BC bottom module (4AccA3:1AccE5), non-uniform refinement of full data set), EMD-56314 (LCC complex bound to palmitoyl-CoA and propionyl-CoA, non-uniform refinement (consensus map)), EMD-56315 (LCC complex bound to palmitoyl-CoA and propionyl-CoA, non-uniform refinement (focused map of top BC module and centre CT module)), EMD-56317 (LCC complex bound to palmitoyl-CoA and propionyl-CoA, non-uniform refinement (focused map of bottom BC module and centre CT module)), EMD-56318 (LCC complex bound to palmitoyl-CoA and propionyl-CoA, local refinement (focused map of centre CT module)), EMD-56320 (LCC complex bound to palmitoyl-CoA and propionyl-CoA, local refinement (focused map of top BC module)), EMD-56321 (LCC complex bound to palmitoyl-CoA and propionyl-CoA, local refinement (focused map of bottom BC module)), **EMD-56323** (LCC complex bound to palmitoyl-CoA and propionyl-CoA, composite map), **EMD-56332** (Centre CT module (4AccD5:2AccD4:2AccE5) bound to palmitoyl-CoA and propionyl-CoA, non-uniform refinement of cluster 1 from 3D variability analysis), **EMD-56333** (Centre CT module (4AccD5:2AccD4:2AccE5) bound to propionyl-CoA, non-uniform refinement of cluster 2 from 3D variability analysis), **EMD-56334** (BC top module (4AccA3:1AccE5), non-uniform refinement of full data set), **EMD-56335** (BC bottom module (4AccA3:1AccE5), non-uniform refinement of full data set); and the Protein Data Bank with accession codes **PBD_00009TUV** (LCC complex bound to ADP, and Mg^{2+}), **PDB_00009TV3** (LCC complex bound to palmitoyl-CoA, ADP, and Mg^{2+}), **PBD_00009TWN** (BC top module (4AccA3:1AccE5) bound to ADP, and Mg^{2+}), **PBD_00009TWO** (BC bottom module(4AccA3:1AccE5) bound to ADP, and Mg^{2+}), **PBD_00009TV6** (LCC complex bound to palmitoyl-CoA), **PBD_00009TVS** (Centre CT module (4AccD5:2AccD4:2AccE5) bound to palmitoyl-CoA), **PBD_00009TW5** (Centre CT module (4AccD5:2AccD4)), **PBD_00009TW6** (BC top module (4AccA3:1AccE5) from EM data of LCC complex incubated with palmitoyl-CoA)), **PBD_00009TWI** (BC bottom module (4AccA3:1AccE5) from EM data of LCC complex incubated with palmitoyl-CoA EM data), **PBD_00009TVE** (LCC complex bound to palmitoyl-

CoA and propionyl-CoA), **PBD_00009TVM** (Centre CT module (4AccD5:2AccD4:2AccE5) bound to palmitoyl CoA and propionylCoA), **PBD_00009TVO** (Centre CT module (4AccD5:2AccD4:2A ccE5) bound to propionyl-CoA), **PBD_00009TVP** (BC top module (4AccA3:1AccE5) from EM data of LCC complex incubated with palmitoyl-CoA and propionyl-CoA), **PBD_00009TVQ** (BC bottom module (4AccA3:1AccE5) from EM data of LCC complex incubated with palmitoyl-CoA and propionyl-CoA).

Acknowledgments

We thank Hans van den Elst for assistance with mass spectrometry, Patrick Voskamp for laboratory support, Kanwal Kayastha for advice on data processing at Leiden Institute of Chemistry. We also thank Willem Noteborn and Ludovic Renault (Netherlands Centre for Electron Nanoscopy) for support with cryo-EM data collection.

This work was supported by the Leiden Institute of Chemistry and by Oncode Accelerator, a Dutch National Growth Fund project under grant number NGFPO2201. It benefited from access to the Netherlands Centre for Electron Nanoscopy (NeCEN) as part of the Netherlands Electron Microscopy Infrastructure (project no. 184.034.014) of the National Roadmap for Large-Scale Research Infrastructure of the Dutch Research Council.

Author contributions: A.Y. and S.G. designed research; A.Y. and B.F. performed research; A.Y. performed the biochemistry, sample preparation, grid screening, image processing and reconstructions and build the model; B.F. performed LC MS, A.Y., N.R., B.F., S.G. analyzed data; A.Y., N.R.,B.F. and S.G. wrote the paper. The authors declare no competing interest.

Material & Correspondence

Correspondence and requests for materials should be addressed to: Sebastian Geibel (s.r.j.@lic.leidenuniv.nl).

References

1. Daffé, M. & Marrakchi, H. Unraveling the Structure of the Mycobacterial Envelope. *Microbiology Spectrum* **7**, 10.1128/microbiolspec.gpp3-0027-2018 (2019).
2. Hoffmann, C., Leis, A., Niederweis, M., Plitzko, J. M. & Engelhardt, H. Disclosure of the mycobacterial outer membrane: Cryo-electron tomography and vitreous sections reveal the lipid bilayer structure. *Proceedings of the National Academy of Sciences* **105**, 3963-3967 (2008).
3. Dulberger, C. L., Rubin, E. J. & Boutte, C. C. The mycobacterial cell envelope — a moving target. *Nat Rev Microbiol* **18**, 47-59 (2020).
4. Block, A. M. *et al.* Mycobacterium tuberculosis Requires the Outer Membrane Lipid Phthiocerol Dimycocerosate for Starvation-Induced Antibiotic Tolerance. *mSystems* **8**, e00699-22.
5. Poulton, N. C. & Rock, J. M. Unraveling the mechanisms of intrinsic drug resistance in Mycobacterium tuberculosis. *Front. Cell. Infect. Microbiol.* **12**, (2022).
6. Tong, L. Structure and function of biotin-dependent carboxylases. *Cell Mol Life Sci* **70**, 863-891 (2013).
7. Marrakchi, H., Lanéelle, M.-A. & Daffé, M. Mycolic Acids: Structures, Biosynthesis, and Beyond. *Chemistry & Biology* **21**, 67-85 (2014).
8. Pawełczyk, J. & Kremer, L. The Molecular Genetics of Mycolic Acid Biosynthesis. *Microbiology Spectrum* **2**, 10.1128/microbiolspec.mgm2-0003-2013 (2014).
9. Gande, R. *et al.* The two carboxylases of Corynebacterium glutamicum essential for fatty acid and mycolic acid synthesis. *J Bacteriol* **189**, 5257-5264 (2007).
10. Bazet Lyonnet, B. *et al.* Functional reconstitution of the Mycobacterium tuberculosis long-chain acyl-CoA carboxylase from multiple acyl-CoA subunits. *The FEBS Journal* **284**, 1110-1125 (2017).
11. Lin, T.-W. *et al.* Structure-based inhibitor design of AccD5, an essential acyl-CoA carboxylase carboxyltransferase domain of Mycobacterium tuberculosis. *Proc Natl Acad Sci U S A* **103**, 3072-3077 (2006).
12. Knowles, J. R. The mechanism of biotin-dependent enzymes. *Annu Rev Biochem* **58**, 195-221 (1989).
13. Attwood, P. V. & Wallace, J. C. Chemical and Catalytic Mechanisms of Carboxyl Transfer Reactions in Biotin-Dependent Enzymes. *Acc. Chem. Res.* **35**, 113-120 (2002).

14. Oh, T.-J., Daniel, J., Kim, H.-J., Sirakova, T. D. & Kolattukudy, P. E. Identification and Characterization of Rv3281 as a Novel Subunit of a Biotin-dependent Acyl-CoA Carboxylase in *Mycobacterium tuberculosis* H37Rv*. *Journal of Biological Chemistry* **281**, 3899-3908 (2006).
15. Pawelczyk, J., Viljoen, A., Kremer, L. & Dziadek, J. The influence of AccD5 on AccD6 carboxyltransferase essentiality in pathogenic and non-pathogenic Mycobacterium. *Sci Rep* **7**, 42692 (2017).
16. Gago, G., Kurth, D., Diacovich, L., Tsai, S.-C. & Gramajo, H. Biochemical and Structural Characterization of an Essential Acyl Coenzyme A Carboxylase from Mycobacterium tuberculosis. *J Bacteriol* **188**, 477-486 (2006).
17. Bennett, M. & Högbom, M. Crystal structure of the essential biotin-dependent carboxylase AccA3 from Mycobacterium tuberculosis. *FEBS Open Bio* **7**, 620-626 (2017).
18. Punjani, A. & Fleet, D. J. 3D variability analysis: Resolving continuous flexibility and discrete heterogeneity from single particle cryo-EM. *J Struct Biol* **213**, 107702 (2021).
19. Huang, C. S. *et al.* Crystal structure of the α6β6 holoenzyme of propionyl-coenzyme A carboxylase. *Nature* **466**, 1001-1005 (2010).
20. Huang, C. S., Ge, P., Zhou, Z. H. & Tong, L. An unanticipated architecture of the 750-kDa α6β6 holoenzyme of 3-methylcrotonyl-CoA carboxylase. *Nature* **481**, 219-223 (2011).
21. Su, J. *et al.* Structural insight into synergistic activation of human 3-methylcrotonyl-CoA carboxylase. *Nat Struct Mol Biol* **32**, 73-85 (2025).
22. Ehebauer, M. T. *et al.* Characterization of the Mycobacterial Acyl-CoA Carboxylase Holo Complexes Reveals Their Functional Expansion into Amino Acid Catabolism. *PLOS Pathogens* **11**, e1004623 (2015).
23. Zhou, F. *et al.* Structural insights into human propionyl-CoA carboxylase (PCC) and 3-methylcrotonyl-CoA carboxylase (MCC). *eLife* **13**, (2024).
24. Liu, Y., Budelier, M. M., Stine, K. & St. Maurice, M. Allosteric regulation alters carrier domain translocation in pyruvate carboxylase. *Nat Commun* **9**, 1384 (2018).
25. Diacovich, L. *et al.* Crystal Structure of the β-Subunit of Acyl-CoA Carboxylase: Structure-Based Engineering of Substrate Specificity,. *Biochemistry* **43**, 14027-14036 (2004).
26. Xiang, S. & Tong, L. Crystal structures of human and Staphylococcus aureus pyruvate carboxylase and molecular insights into the carboxyltransfer reaction. *Nat Struct Mol Biol* **15**, 295-302 (2008).

27. Filament structures unveil the dynamic organization of human acetyl-CoA carboxylase. *Science Advances* https://www.science.org/doi/10.1126/sciadv.ado4880.
28. Abramson, J. *et al.* Accurate structure prediction of biomolecular interactions with AlphaFold 3. *Nature* **630**, 493-500 (2024).
29. Shevchenko, A., Tomas, H., Havlis, J., Olsen, J. V. & Mann, M. In-gel digestion for mass spectrometric characterization of proteins and proteomes. *Nat Protoc* **1**, 2856-2860 (2006).
30. Punjani, A., Rubinstein, J. L., Fleet, D. J. & Brubaker, M. A. cryoSPARC: algorithms for rapid unsupervised cryo-EM structure determination. *Nat Methods* **14**, 290-296 (2017).
31. Punjani, A., Zhang, H. & Fleet, D. J. Non-uniform refinement: adaptive regularization improves single-particle cryo-EM reconstruction. *Nat Methods* **17**, 1214-1221 (2020).
32. Jamali, K. *et al.* Automated model building and protein identification in cryo-EM maps. *Nature* **628**, 450-457 (2024).
33. Pettersen, E. F. *et al.* UCSF ChimeraX: Structure visualization for researchers, educators, and developers. *Protein Sci* **30**, 70-82 (2021).
34. Afonine, P. V. *et al.* Real-space refinement in PHENIX for cryo-EM and crystallography. *Acta Crystallogr D Struct Biol* **74**, 531-544 (2018).
35. Liebschner, D. *et al.* Macromolecular structure determination using X-rays, neutrons and electrons: recent developments in Phenix. *Acta Crystallogr D Struct Biol* **75**, 861-877 (2019).
36. Emsley, P., Lohkamp, B., Scott, W. G. & Cowtan, K. Features and development of Coot. *Acta Crystallogr D Biol Crystallogr* **66**, 486-501 (2010).
37. Janiyani, K., Bordelon, T., Waldrop, G. L. & Cronan, J. E. Function of Escherichia coli Biotin Carboxylase Requires Catalytic Activity of Both Subunits of the Homodimer. *Journal of Biological Chemistry* **276**, 29864-29870 (2001).

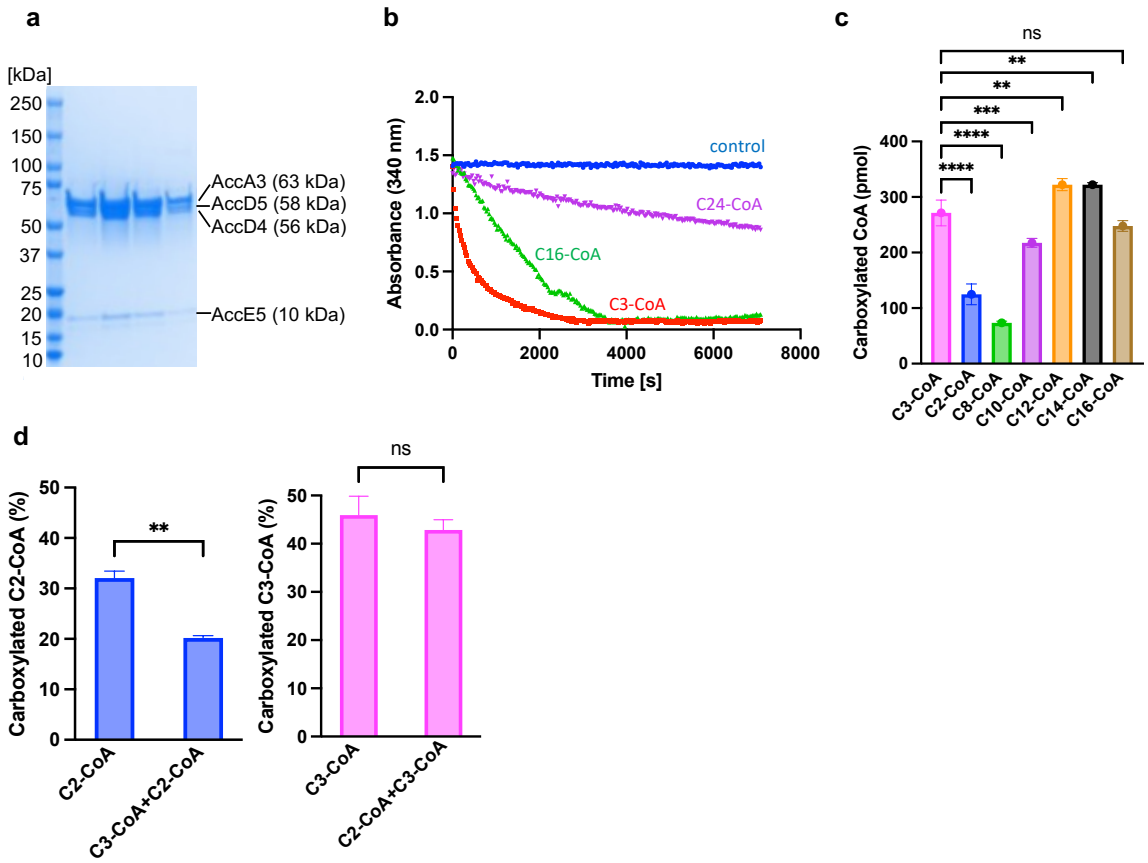

Figure 1. Purification and biochemical characterization of endogenous LCC.

a, SDS-PAGE analysis of the long-chain acyl-CoA carboxylase (LCC) complex purified from *Mycobacterium smegmatis*.

b, ATPase activity of purified LCC measured in the presence of propionyl-CoA (C3-CoA), palmitoyl-CoA (C16-CoA), or lignoceroyl-CoA (C24-CoA).

c, Quantification of carboxylated acyl-CoA species (C2-, C3-, C8-, C10-, C12-, C14-, and C16-CoA) by IP-RP-HPLC-ESI-TQMS/MS. Statistical significance was assessed by one-way ANOVA ($P < 0.0001$) followed by Dunnett's multiple-comparisons test (reference, C3-CoA; ****$P < 0.0001$, ***$P < 0.001$, **$P < 0.01$; ns, not significant).

d, Substrate-competition assay measuring carboxylation of C2-CoA and C3-CoA in the presence of the competing substrate. Welch's unpaired two-tailed *t*-test was used (**$P < 0.01$; ns, not significant). Data are mean ± s.d. (n = 3).

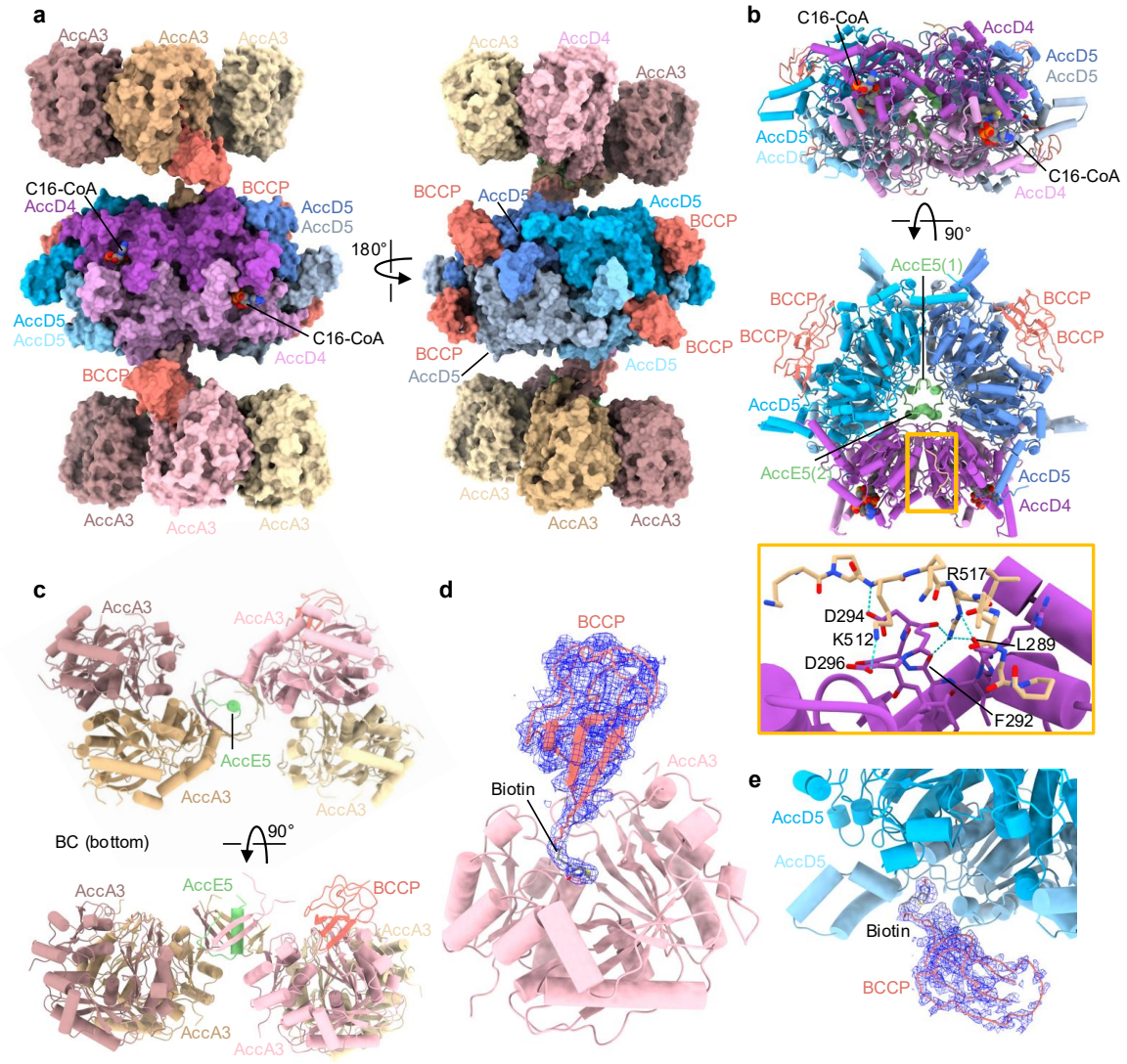

Figure 2. Pre-activation state of LCC bound to palmitoyl-CoA.

a, Surface representation of the LCC complex derived from a composite cryo-EM reconstruction (Supplementary Fig. 4). The central carboxyltransferase (CT) core is flanked by two biotin carboxylase (BC) modules connected by AccE5 linker subunits. Palmitoyl-CoA (sphere representation) is bound at the two active sites formed by the AccD4 dimer (purple). Left, view showing BCCP domains (salmon) associated with the upper and lower BC modules. Right, view rotated by 180° showing BCCP domains positioned near the AccD5-facing surface (blue) of the CT core.

b, Side and top views of the CT module composed of two AccD4 (purple) and four AccD5 (blue) protomers. The C-terminal helix-turn-helix motif of AccE5 (green) is positioned within the CT-ring lumen, and a loop from AccA3 (yellow) contacts AccD4 (inset). Hydrogen bonds are indicated by blue dashed lines.

c, Top and side views of the BC module composed of four AccA3 protomers (brown, orange, pink, and yellow). The N-terminal α-helix of AccE5 (green) is inserted into a β-barrel structure formed by the AccA3 tetramer and AccE5.

d, Cryo-EM density (blue mesh) corresponding to a BC-associated BCCP (salmon), with the biotinylated Lys564 positioned within the ATP-binding pocket of one AccA3 protomer (pink).

e, Cryo-EM density (blue mesh) corresponding to a CT-proximal BCCP (salmon), with the biotinylated Lys564 positioned near the substrate entry site of AccD5 (blue).

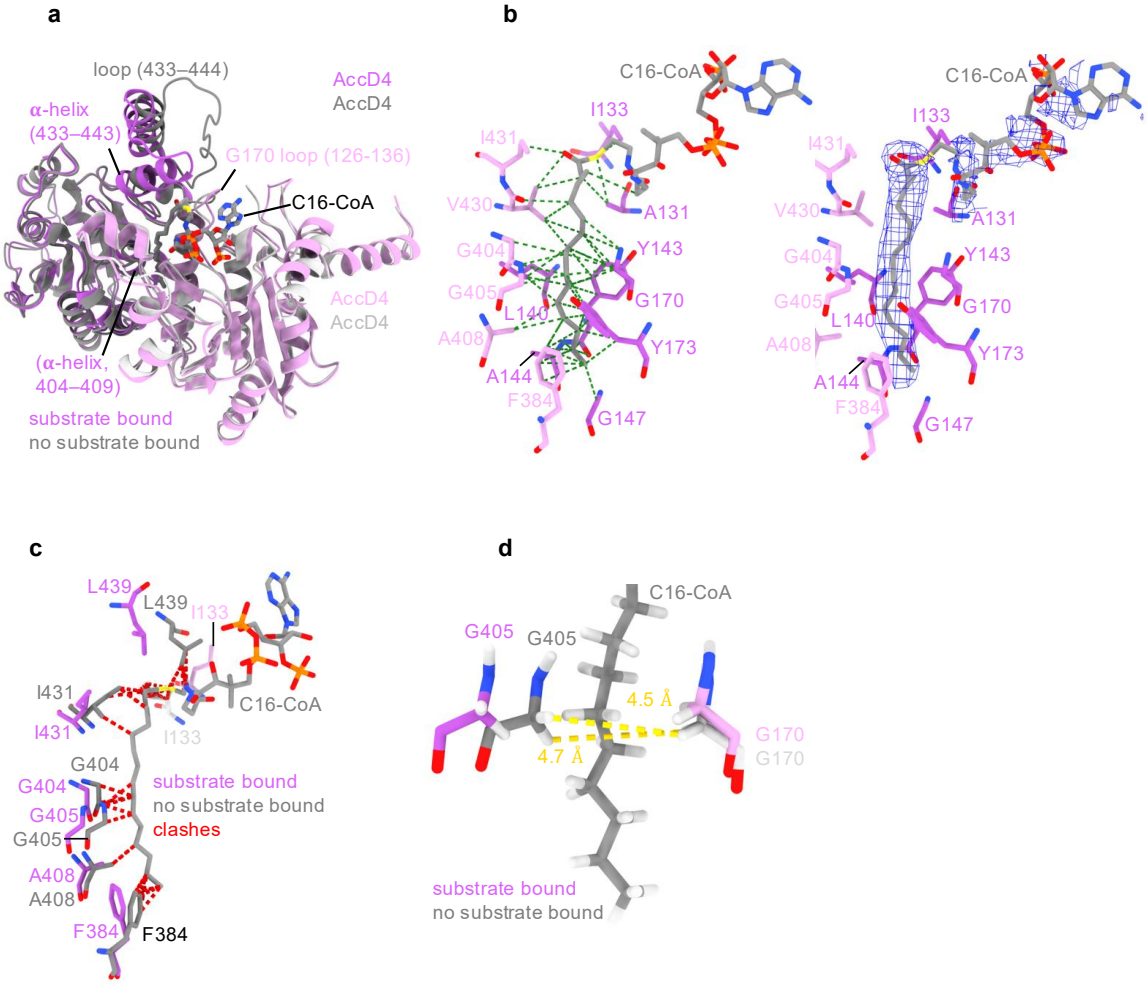

Figure 3. Conformational states of AccD4 associated with long-chain substrate binding.
a, Structural superimposition of AccD4 dimers in a substrate-free, closed conformation (grey) and a substrate-bound, open conformation (magenta). C16-CoA bound to the open AccD4 dimer is shown as a stick model. Secondary-structure elements occluding the substrate-binding site were omitted for clarity.
b, Open conformation of the AccD4 dimer with C16-CoA positioned within the acyl-chain tunnel. Van der Waals contacts between AccD4 and C16-CoA are indicated by green dashed lines; the right panel shows cryo-EM density corresponding to C16-CoA (blue mesh).
c, Superimposition of the closed, substrate-free AccD4 dimer with the open, C16-CoA-bound conformation. Steric clashes between C16-CoA and surrounding residues in the closed conformation are indicated by red dashed lines.
d, Comparison of the open and closed AccD4 conformations highlighting inward shift of residue G405 in the closed conformation and the resulting narrowing of the acyl-chain tunnel. The CoA moiety and part of the acyl chain were omitted for clarity. Distances between hydrogen atoms at the constriction point are indicated by yellow dashed lines.

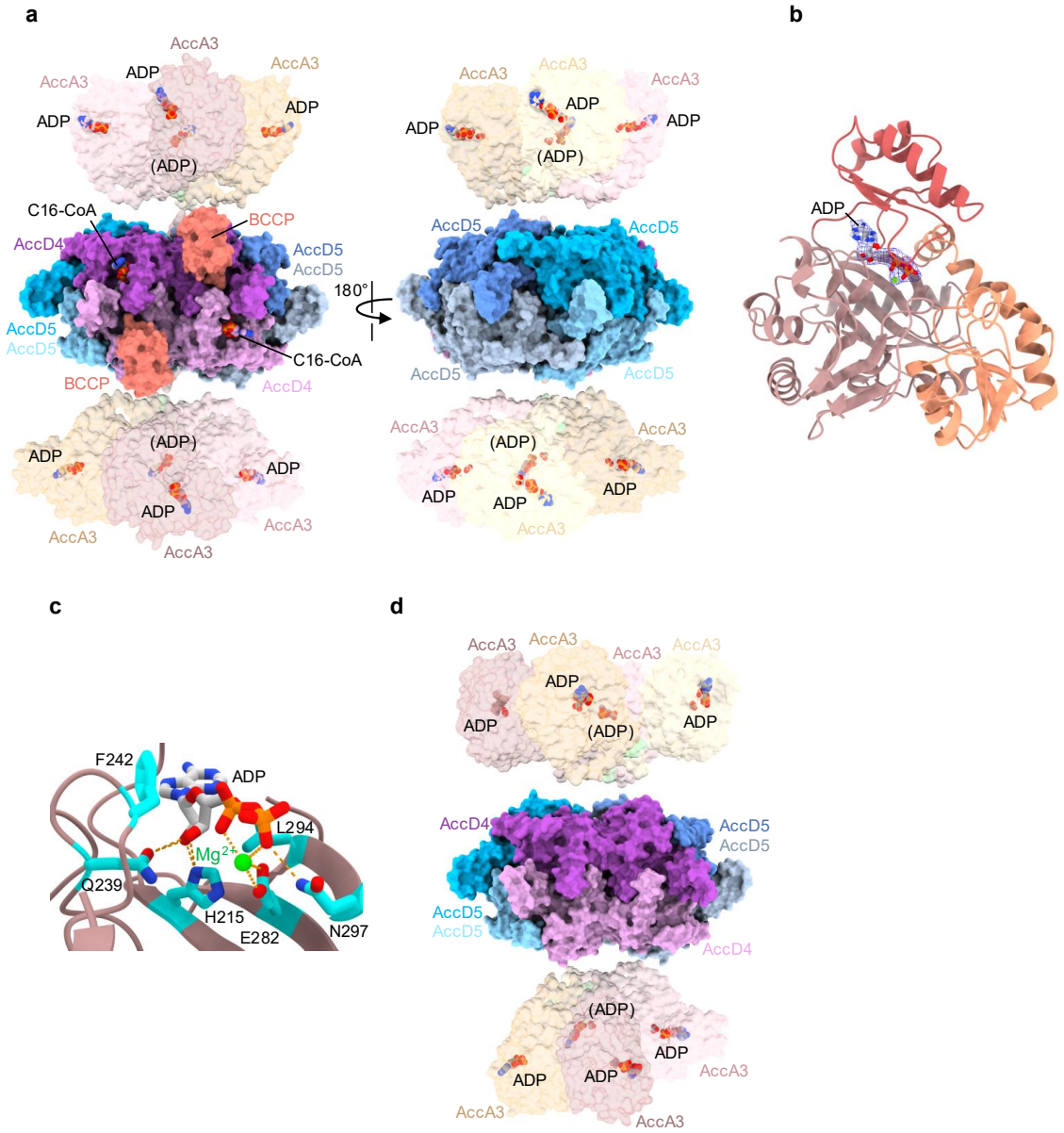

Figure 4. Post-reaction states of LCC under ATP turnover conditions.
a, Post-reaction state 1. Surface representation of LCC derived from a composite cryo-EM reconstruction obtained under ATP turnover conditions (Supplementary Fig. 9). C16-CoA, shown as spheres, is bound at the two active sites formed by the AccD4 dimer (purple). BCCP domains (salmon) are positioned proximal to AccD4, and ADP-Mg^{2+} is bound to AccA3 protomers within the biotin carboxylase (BC) modules, which are rendered transparent to visualize the nucleotide. A view rotated by 180° is shown on the right. No BCCP density is observed at AccD5 (blue).
b, Atomic model of an AccA3 monomer with bound ADP-Mg^{2+} from post-reaction state 1; the BCCP domain is omitted for clarity. Cryo-EM density corresponding to ADP-Mg^{2+} is shown as a blue mesh.
c, Close-up view showing interactions between ADP-Mg^{2+} and active-site residues of AccA3.
d, Post-reaction state 2. Surface representation of LCC derived from a composite cryo-EM reconstruction of a substrate-release state under ATP turnover conditions (Supplementary Fig. 13), with ADP-Mg^{2+} retained at the AccA3 active sites.

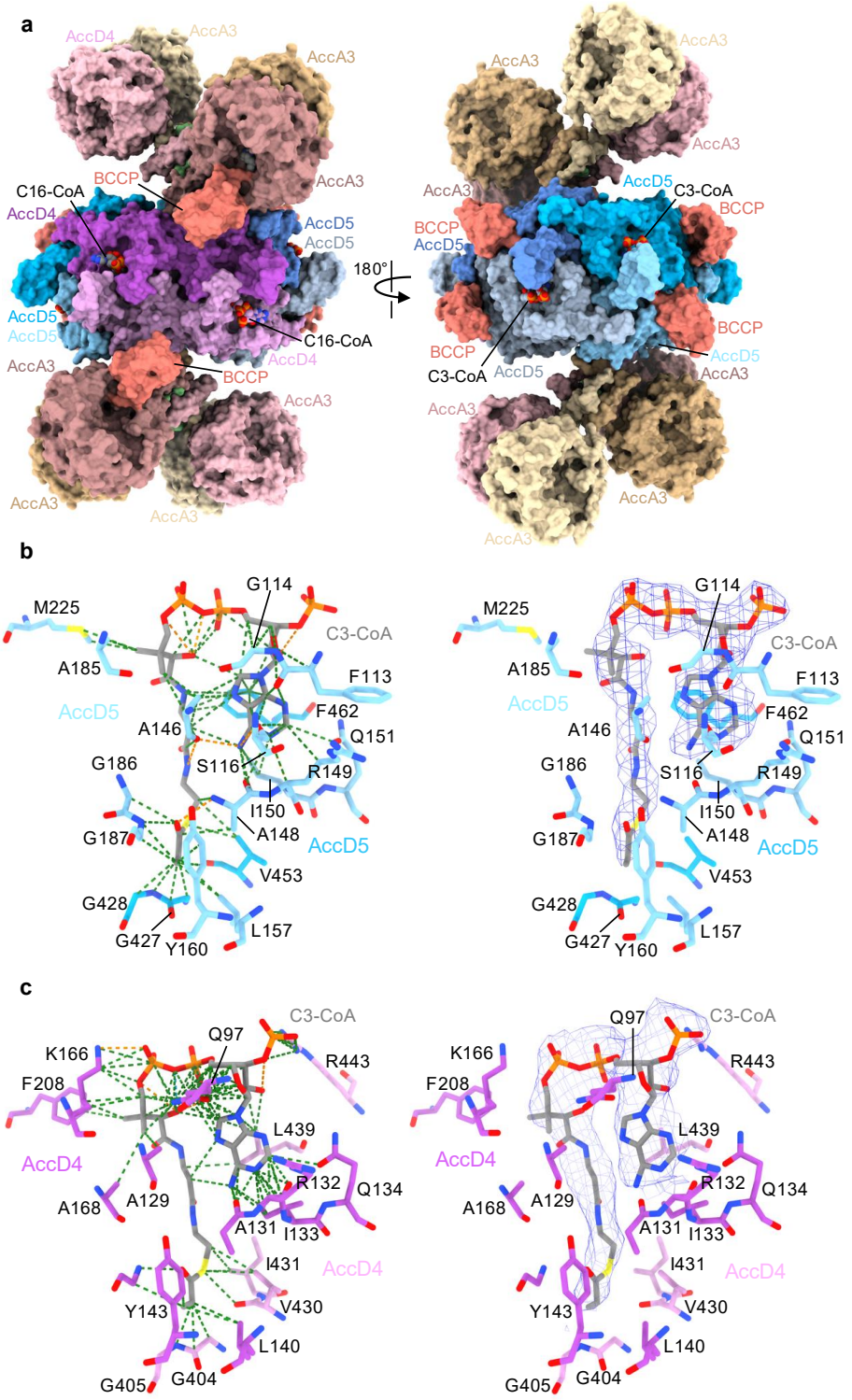

Figure 5. Pre-activation state of LCC bound to both C3-CoA and C16-CoA.

a, Surface representation of LCC derived from a composite cryo-EM reconstruction (Supplementary Fig. 16). C3-CoA and C16-CoA, shown as spheres, are bound at active sites formed by AccD5 dimers (blue) and the AccD4 dimer (purple), respectively. Left, view showing BCCP domains (salmon) associated with the biotin carboxylase (BC) modules. Right, view rotated by 180° showing BCCP domains positioned near the AccD5-facing surface of the carboxyltransferase (CT) core.

b, Close-up view of the AccD5 active site bound to C3-CoA. Hydrogen bonds are indicated by orange dashed lines and van der Waals contacts by green dashed lines; the right panel shows cryo-EM density corresponding to C3-CoA (blue mesh).
c, Close-up view of the AccD4 active site with C3-CoA bound in the closed conformation. Hydrogen bonds are indicated by orange dashed lines and van der Waals contacts by green dashed lines; the right panel shows cryo-EM density corresponding to C3-CoA (blue mesh).

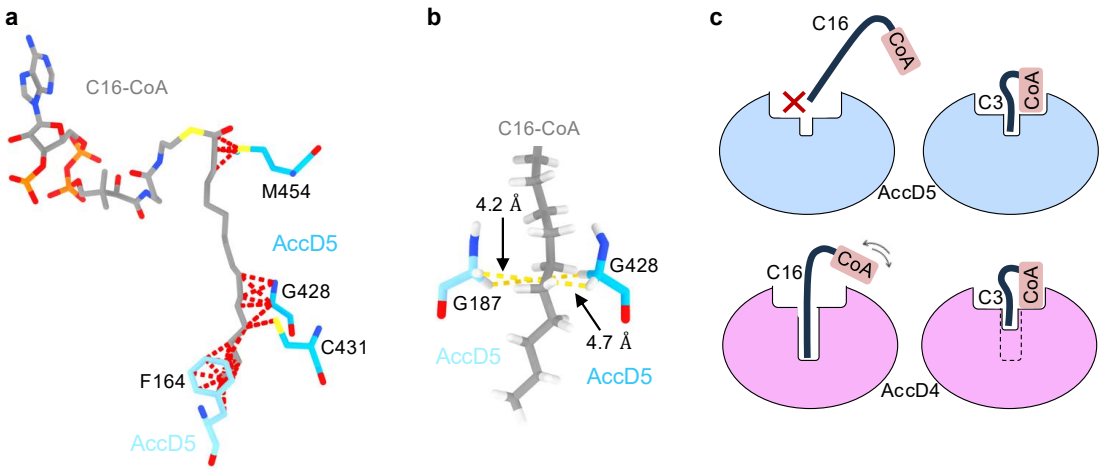

Figure 6. Structural basis of substrate selectivity in AccD4 and AccD5.
a, Superimposition of the C16-CoA-bound AccD4 dimer with the C3-CoA-bound AccD5 dimer. The position of the C16 acyl chain relative to the AccD5 active site is shown, with steric overlap between the acyl chain and surrounding AccD5 residues indicated by red dashed lines (AccD5 dimer shown in blue). CoA moiety and part of the acyl chain were omitted for clarity.
b, Close-up view of the AccD5 active site highlighting residues G187 and G428, which define a constriction within the acyl-chain tunnel (AccD5 shown in blue). CoA moiety and part of the acyl chain were omitted for clarity.
c, Schematic summary of substrate selectivity, illustrating that AccD5 (blue) accommodates C3-CoA but not C16-CoA, whereas AccD4 (purple) binds C16-CoA in the open conformation and C3-CoA in the closed conformation.

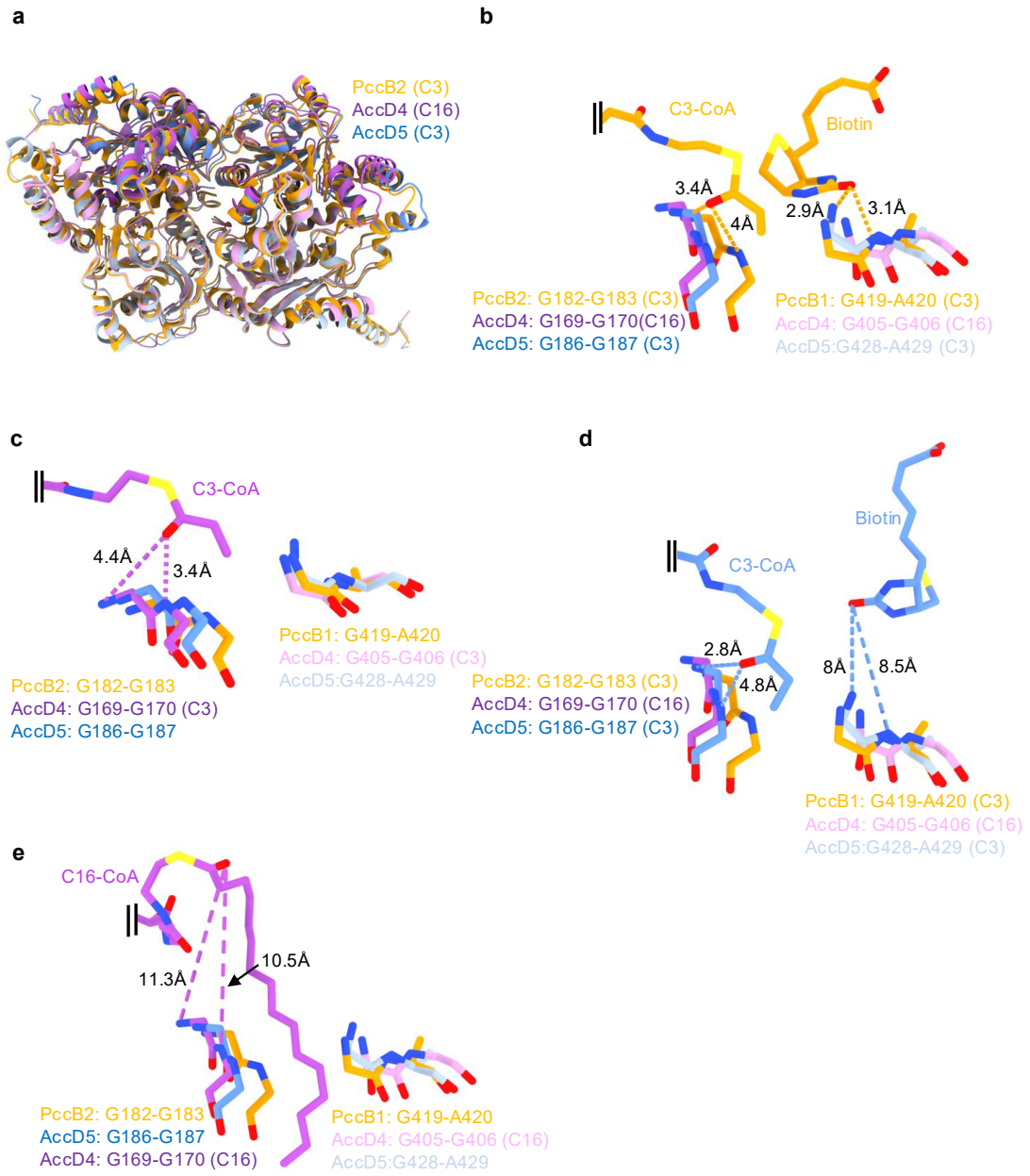

Figure 7. Comparison of ligand positioning relative to conserved oxyanion holes in PccB, AccD4, and AccD5.

a, Structural superposition of the C3-CoA-bound PccB dimer from *Streptomyces coelicolor* (PDB: 1XNY) with the C3-CoA-bound AccD5 dimer (blue) and the C16-CoA-bound AccD4 dimer (purple).

b-e, Following structural superposition of PccB, AccD4, and AccD5, conserved oxyanion-hole residues from all three enzymes occupy structurally equivalent positions and are shown as stick representations. Close-up views show **b,** C3-CoA and biotin bound to the PccB dimer (orange); **c,** C3-CoA bound to the AccD4 dimer (purple); **d,** C3-CoA and biotin bound to the AccD5 dimer (blue); and **e,** C16-CoA bound to the AccD4 dimer (purple). Distances between the ligands and the oxyanion holes are indicated.

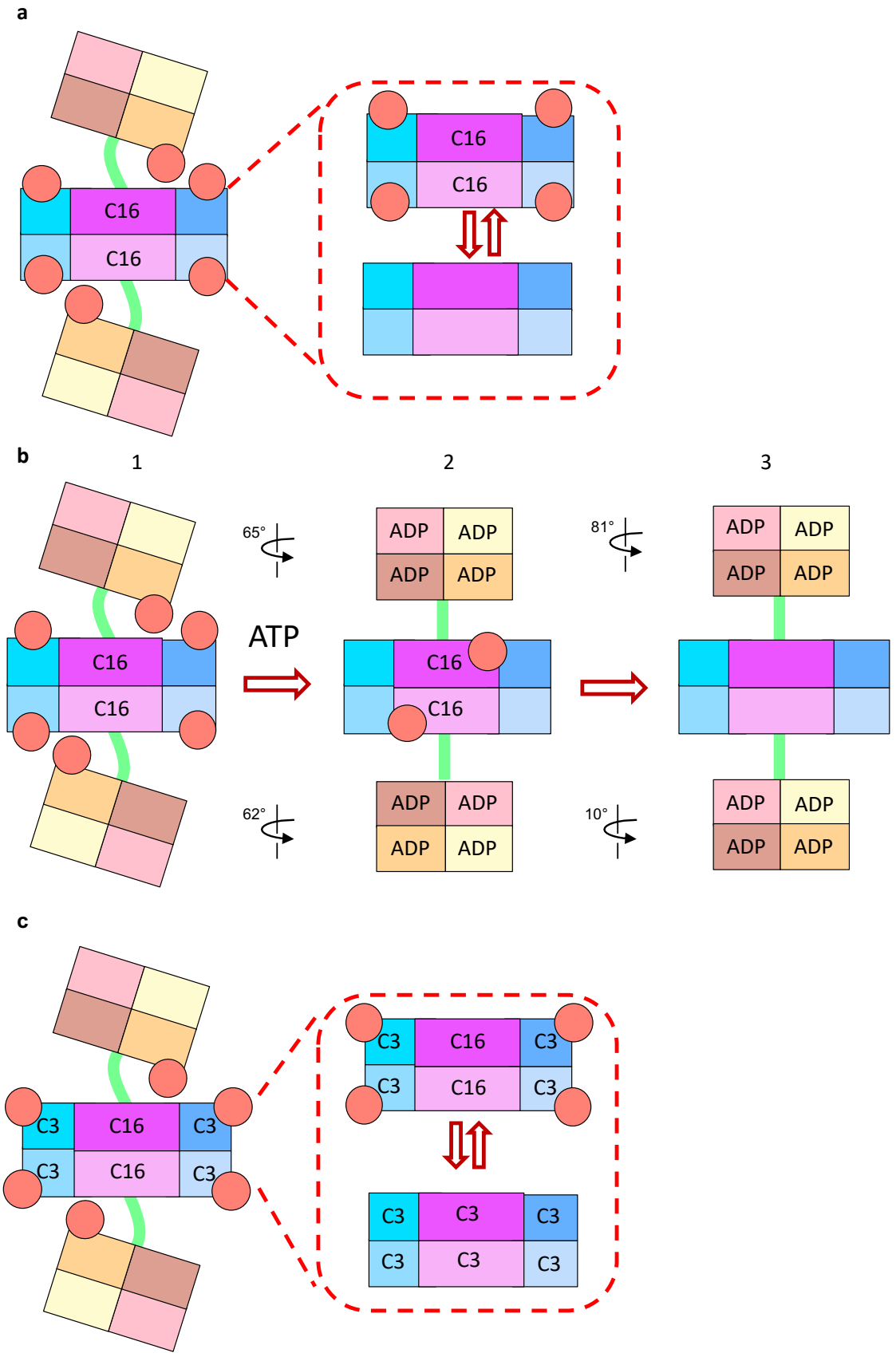
a
C16
C16
C16
C16
b
1
2
3
65°
ATP
62°
81°
10°
ADP
ADP
ADP
ADP
C16
C16
c
C3
C16
C3
C3
C16
C3
C3
C16
C3
C3
C16
C3
C3
C3
C3
C3
C3
C3

Figure 8. Schematic overview of conformational dynamics of LCC.
a, LCC bound to C16-CoA in the absence of ATP. The carboxyltransferase (CT) module adopts two conformations: an open, C16-CoA-bound state (top, inset) and a closed, apo state (bottom, inset). Although C16-CoA is bound at the AccD4 dimer active site, BCCP samples positions between the biotin carboxylase (BC) modules and the CT module.
b, Conformational changes in LCC upon ATP binding. BCCP dissociates from the BC modules and associates with the C16-CoA-bound AccD4 dimer active site (purple) within the CT module, while ADP bound at the BC modules marks a post-carboxylation state of the BCCP biotin. Carboxylation of C16-CoA is not captured in the CT module. Rotation of the upper and lower BC modules by ~62-65° positions the BCCP domains (salmon), consistent with shuttling between the BC and CT modules. A subsequent post-reaction state shows the CT module in an apo conformation while the BC modules remain ADP-bound, with BCCPs dissociated from both modules. Additional BC-module rotations of ~81° and ~10° are observed.
c, LCC bound simultaneously to C3-CoA and C16-CoA. Two CT-module conformations are illustrated. In the open state (top, inset), the AccD4 dimer (purple) binds C16-CoA while the AccD5 dimers (blue) bind C3-CoA. In the closed state of the AccD4 dimer (bottom, inset), both AccD4 and AccD5 bind C3-CoA.